Improving the CT (140 kVp) to PET (511 keV) conversion in PET/MR Hardware Component Attenuation Correction

Short running title: Improved PET/MR attenuation correction

Mark Oehmigen[1], Maike E. Lindemann[1], Lutz Tellmann[2], Titus Lanz[3] and Harald H. Quick[1, 4]

[1]*High-Field and Hybrid MR Imaging, University Hospital Essen, Essen, Germany*

[2]*Institute for Neuroscience and Medicine (INM-4), Forschungszentrum Jülich GmbH, Jülich, Germany*

[3]*Rapid Biomedical GmbH, Rimpar, Germany*

[4]*Erwin L. Hahn Institute for MR Imaging, University Duisburg-Essen, Essen, Germany*

Send correspondence requests to:

Mark Oehmigen, MSc

High-Field and Hybrid MR Imaging

University Hospital Essen

Hufelandstr. 55, 45147 Essen, Germany

Tel.: +49 201 723 84534

E-mail: mark.oehmigen@uni-due.de

Abstract

Purpose

Today, attenuation correction (AC) of PET/MR hardware components is performed by using an established method from PET/CT hybrid imaging. As shown in previous studies, the established mathematical conversion from CT to PET attenuation coefficients may, however, lead to incorrect results in PET quantification when applied to AC of hardware components in PET/MR. The purpose of this study is to systematically investigate the attenuating properties of various materials and electronic components frequently used in the context of PET/MR hybrid imaging. The study, thus, aims at improving hardware component attenuation correction in PET/MR.

Material and Methods

Overall, 38 different material samples were collected; a modular phantom was used to for CT, PET, and PET/MR scanning of all samples. CT-scans were acquired with a tube voltage of 140 kVp to determine Hounsfield Units (HU). PET transmission scans were performed with 511 keV to determine linear attenuation coefficients (LAC) of all materials. The attenuation coefficients were plotted to obtain an HU to LAC correlation graph, which was then compared to two established conversions from literature. Hardware attenuation maps of the different materials were created and applied to PET data reconstruction following a phantom validation experiment. From these measurements, PET difference maps were calculated to validate and compare all three conversion methods.

Results

For each material, the HU and corresponding LAC could be determined and a bi-linear HU to LAC conversion graph was derived. The corresponding equation was $y = 1.64 * 10^{-5} \times (\mathrm{HU} + 1000) +$

$8.3 * 10^{-2}$. While the two established conversions lead to a mean quantification PET bias of 4.69 % ± 0.27 % and -2.84 % ± 0.72 % in a phantom experiment, PET difference measurements revealed only 0.5 % bias in PET quantification when applying the new conversion resulting from this study.

Conclusion

An optimized method for the conversion of CT to PET attenuation coefficients has been derived by systematic measurement of 38 different materials. In contrast to established methods, the new conversion also considers highly attenuating materials, thus improving attenuation correction of hardware components in PET/MR hybrid imaging.

Keywords

PET/MR, attenuation correction (AC), Hounsfield unit (HU), linear attenuation coefficient (LAC)

Introduction

Since its introduction in 2010, simultaneous positron emission tomography/magnetic resonance (PET/MR) has found its way into various clinical applications ranging from neuro to pediatric and cardiac to whole-body applications in oncology.[1,2,3,4] Recent studies also work towards the integration of PET/MR hybrid imaging into the concept of radiation therapy planning.[5,6] All of these PET/MR applications have in common, that for high-quality PET and MR imaging dedicated hardware is required: radiofrequency (RF) coils, phantoms, positioning aids, and table platforms.[7,8,9,10,11,12]

During simultaneous PET and MR data acquisition, these hardware components are positioned in the field-of-view (FOV) of the PET detector and attenuate the PET annihilation photons. This may lead to visible artifacts and bias in PET quantification.[11] Consequently, all PET signal attenuation caused by hardware components and patient tissue needs to be corrected using appropriate attenuation correction (AC) methods. These AC methods in PET/MR are fundamentally different compared to PET/CT hybrid imaging. Attenuation correction in PET/MR is generally performed with two different approaches. Photon attenuation due to human tissues is based on MR imaging using dedicated AC sequences that provide a segmentation into different tissue classes and then assign linear attenuation coefficients (LAC) for each tissue class .[13,14,15,16] Photon attenuation due to hardware components, on the other hand, is based on CT scans of the respective hardware component .[17,18] The CT data is then converted with dedicated conversion curves to the energy level of the PET component.[19] Both methods for AC in PET/MR are thus different from AC in PET/CT. CT can provide high-resolution transmission scans. In PET/CT these CT scans represent the spatial distribution of attenuating human tissues and hardware components such as the PET/CT patient table, phantoms, and further table platforms. Furthermore, PET signal attenuating RF coils are not needed for signal reception in PET/CT.

Today, the AC of human tissues in PET/MR is usually solved by applying dedicated MR sequences, subsequent tissue segmentation integrating bone models, atlas-based methods and the emission-based estimation of attenuation.[13,14,15,16,20,21] Moreover, joint reconstruction algorithms add to the palette of methods for human tissue AC, and deep learning now enters the field to provide MR-derived pseudo-CT data for AC of human tissues.[22,23]

However, AC of hardware components such as RF coils, phantoms, and radiation therapy (RT) equipment has to be performed differently, since all these components and materials are not visible in MR imaging and thus cannot be segmented and assigned with attenuation coefficients. The established approach in PET/MR is to acquire CT-based three-dimensional (3D) virtual attenuation models of the respective hardware component (e.g. RF coil).[24,25] These CT-based AC templates represent the spatial distribution of attenuation values in Hounsfield units (HU), acquired at a specific CT tube voltage of e.g. 140 kVp. The attenuation values of the CT-based AC template are then converted to linear attenuation coefficients (LAC) at 511 keV PET energy levels. This method for hardware AC in PET/MR resembles the established method for attenuation correction in PET/CT.

Numerous mathematical HU to LAC conversion methods have been suggested for application in PET/CT, including bilinear conversion curves, quadratic polynomial calibration curve, dual-energy CT and conversions based on virtual dual-energy CT data (VDECT).[26,27,28,29] All these methods aim at accurate conversion of the measured CT data, e.g. acquired at 80 – 140 kVp, to proper linear attenuation coefficients (LAC) at 511 keV energy level of PET data. Accurate conversion, thus, is a precondition to obtaining accurate quantification of PET data following AC. The bi-linear conversion methods proposed by Kinahan et al. and Carney et al. today are routinely established in PET/CT hybrid imaging and work fast, accurate and robust for AC of patient tissues and phantom measurements in PET/CT.[17,18]

While the established conversions work well in PET/CT, all these methods only focused on the conversion of lower attenuation values of human tissues and are not optimized for the correction of

higher attenuating materials and metals.[18,19,26,27,28,29] With the advent of the PET/MR systems, however, additional hardware components such as the patient table and radiofrequency coils and further materials may present higher attenuation values than human tissues. Thus, Paulus et al., in their study extended the HU scale during CT acquisition towards higher attenuating materials (up to 30000 HU).[19] The study by Paulus et al. demonstrated, that considering also the stronger attenuating hardware components and materials results in an adapted slope of the curve provided by Carney et al. and therefore reduces bias in CT-based attenuation maps of hardware components for use in PET/MR applications.[18,19]

Building on the findings by Paulus et al., this study aims to provide an optimized conversion curve for AC of ancillary hardware components in PET/MR hybrid imaging. Varying materials ranging from plastics and metals, as well as electronic components and cables, were systematically investigated. The use of these diverse materials can all be found in the manufacture of RF coils, phantoms, and other ancillary hardware. The attenuating properties of 38 different material probes were investigated in both 140 kVp CT scans and 511 keV PET transmission scans. A new HU-to-LAC-conversion curve was derived and compared to the established conversion curves.[18,19] The results of this study lead to an adapted and improved HU-to-LAC conversion curve that also considers highly attenuating materials and, consequently, further improves the accuracy of AC of the hardware setup in PET/MR hybrid imaging.

Material and Methods

Material samples

A total of 38 material samples were examined. All material samples were provided by a RF coil manufacturer (Rapid Biomedical GmbH, Rimpar, Germany) and include various plastics, metals, cables, and electronic components commonly used in PET/MR phantom housing and RF coil manufacturing. The material samples were divided into two major groups of 19 samples each (Figure

1). The first group comprises heterogeneous samples (#1-#19), mainly electronic components, including ceramic capacitors of different sizes, cables, soldering tin, inductors, small RF preamplifiers, and others. The second group includes solid and homogeneous samples (#20-#38) like various plastics and metals, such as aluminum, copper, and brass, used for hardware component manufacturing (Figure 1).

Figure 1: Overview of all 38 material samples. Samples #1-#19 (upper row) contain several electronic components and cables; samples #20 - #38 (lower row) are a collection of various homogeneous plastics and metals.

The group of heterogeneous samples includes electronic components that all vary in size and shape. For better comparison between the two groups, thin-walled plastic test tubes with a cylindrical shape and comparable dimensions (16 mm outer diameter, length 200 mm) like the homogeneous samples were selected. The electronic components were filled into the test tubes and sealed with flexible foam, to compress and fixate the small movable electronic components minimizing displacement between experiments.

The homogenous samples (#20 - #38) are each 150 mm long and have a diameter of 16 mm. The unified sample size and cylindrical shape were considered as advantageous regarding handling in phantom experiments: cylindrical shape for uniform photon transmission, and symmetry for designing a modular phantom setup. The entire list of materials and detailed specifications is provided in Table 1.

Table 1 Detailed material list

no.	heterogeneous materials	quantity	no.	homogenous materials	density [g/cm³]
#1	Capacitor, small dimension	940	**#20**	PVC [Polyvinyl chloride]	1.39
#2	Capacitor, medium dimension	120	**#21**	TECAPET [Polyethylene terephthalate]	1.36
#3	Capacitor, large dimension	37	**#22**	Copper	8.91
#4	Soldering tin	90	**#23**	PC [Polycarbonate]	1.19
#5	Cable, K02252	19	**#24**	PMMA [Polymethyl methacrylate]	1.19
#6	Cable, 6Y-C6Y	90	**#25**	POM [Polyoxymethylene]	1.43
#7	Cable, DC wire	130	**#26**	GFK [Glass fiber reinforced epoxy]	1.92
#8	Cable 1TX / 8RX	1	**#27**	2-K Epoxid [Epoxy resin]	1.09
#9	Cable 2TX/2RX/6DC	2	**#28**	PEI [Polyethylenimine]	1.26
#10	Inductor, large dimension	39	**#29**	Aluminium	2.69
#11	Inductor, small dimension	165	**#30**	PPSU [Polyphenylsulfon]	1.29
#12	glass reinforced printed circuit board	1	**#31**	Brass	8.46
#13	Printed circuit board FR4, one-sided	1	**#32**	PEEK [Polyether ether ketone]	1.32
#14	Midi Spring Inductor	135	**#33**	PA [Polyamide]	0.93
#15	Inductor 4700 nH	640	**#34**	PS [Polystyrene]	1.06
#16	Transceive trimmable inductor	11	**#35**	PE [Polyethylen]	1.13
#17	PIN diode [Positive intrinsic negative diode]	65	**#36**	PVDF [Polyvinylidine fluoride]	1.79
#18	Preamplifier	6	**#37**	ABS [Acrylonitrile-butadiene-styrene]	1.06
#19	PUR SG95 SLM [Polyurethane]	1	**#38**	PUR [Polyurethane]	1.26

Table 1: Overview of specific material parameters of samples #1-38.

Phantom design

A phantom was designed that allows for reproducible transmission measurements of all 38 material samples in CT and PET systems. Polystyrene (PS) foam was selected so it would not significantly influence the CT and PET transmission measurements due to its mechanically stable but rather low-attenuating properties. The average HU for the PS material was determined to be -900, which is close to the HU of air (HU -1000). An annular-shaped holder was chosen to permit the equidistant and symmetric arrangement of the samples around the isocenter axis of the respective CT, PET, and PET/MR systems during all measurements. Through the process of water jet cutting, the PS foam was formed into an annular shape with an inner diameter of 214 mm and an outer diameter of 294 mm. The ring is supported by a little pedestal at the base providing stability during CT, PET, and PET/MR measurements. Two identical annular phantom holders were manufactured and 19 equidistant holes were drilled into the PS foam to provide a reproducible setting for the 19 heterogeneous (Figure 2A) and 19 homogeneous (Figure 2B) material samples.

An inner diameter of 214 mm was chosen for the purpose of allowing the cylindrically shaped water phantom (volume 9480 ml) to be used in conjunction with the overall phantom setting (Figure 2C). Additionally, the water phantom can be filled with radiotracer through ports located on the top lid, thus providing a homogeneous large-volume emission source.

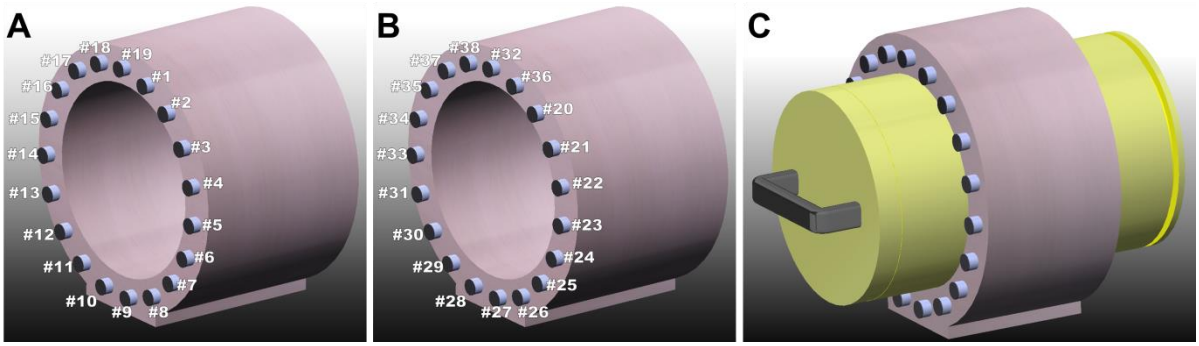

Figure 2: Virtual model of two annular-shaped sample holders *made from low-attenuating foam each provides a reproducible setting for phantom experiments. The sample holder in (A) contains the heterogeneous electronic components #1-19; sample holder (B) contains various homogeneous material samples #20-38 made from*

plastic and metals. Both sample holders (A, B) can be combined with an active large-volume water phantom for PET emission measurements (C).

CT scans

The two sample holders loaded with all 38 materials were first scanned on a dual-energy CT scanner (SOMATOM Force, Siemens Healthcare GmbH, Erlangen, Germany). The dual-energy option of the CT system was neither needed nor used in this experiment. 140 kVp was chosen for CT energy, which is the highest energy level that is broadly available on all modern CT and PET/CT hybrid imaging systems. This assures the applicability of the results of this study at other institutions as well as comparability to the results of the studies by Carney et al. (21) and by Paulus et al. (22). The following CT imaging parameters were used: tube voltage 140 kVp, tube current 650 mA, matrix size of 512 × 512 pixels, voxel size 0.3 × 0.3 × 0.6 mm^3 and a B30f-smooth convolution kernel. Reconstruction of the CT data was done by applying the extended Hounsfield scale. While the standard CT HU scale ranges from −1024 HU to +3071 HU to include all human body, (background air up to the cortical bone, calcifications, and teeth), the extended CT scale displays HU in steps of ten up to a maximum of +30710 HU. Therefore, most high attenuating materials and hardware components including different metals and ceramics are covered by the extended CT scale.

The CT data for the material samples were examined with VINCI (VINCI Version 4.63, Max-Planck-Institute for Metabolism Research, Cologne, Germany).[30] The aim was to identify the mean HU value for each material sample, scanned with 140 kVp tube voltage. Therefore, the Dicom CT data were overlaid with a region-of-interest (ROI) of 16 mm diameter in the axial view (Figure 3A). The mean HU value for each ROIs, each with a slice thickness of 0.6 mm, was measured over the entire length of the material sample. All mean values of all ROI in each slice were taken into account for determining the overall mean HU value for the specific material (Figure 3A). An additional threshold (-100 HU) for the heterogeneous materials was applied with MATLAB 2013b (MATrix

LABoratory, MathWorks, Massachusetts, USA) using a customized MATLAB tool, to segment and consider only the full material components within the sample tubes and not surrounding air between the individual components.

PET transmission scans

A dedicated PET scanner, ECAT EXACT HR^{+}, Siemens Healthcare GmbH, Erlangen, Germany) equipped with rotating ^{68}Ge/^{68}Ga rod sources (each around 150 MBq) was used to obtain LAC from all materials.[31] The two-dimensional linear attenuation coefficients of all materials are directly measured by the transmission of the rotating line sources while the PET detector was operated in transmission mode.[32] No further attenuation correction or energy conversion had to be applied because the measured attenuation coefficients are the reference LAC values acquired at 511 keV.

For the PET transmission measurements two sample holders with the heterogeneous and homogeneous probes were fixed free-floating at the head end of the patient table and two PET measurements were performed sequentially, one for each sample holder. Acquisition time was more than 150 minutes to obtain a high number of counts and true events. The data were reconstructed applying OSEM (10 iterations, 8 subsets, Gauss filter 6.0 mm) using the e7-tools (Siemens Molecular Imaging, Knoxville, USA) with a matrix of 128 x 128 and 63 slices, resulting in a pixel size of 5.2 x 5.2 mm² and a slice thickness of 2.43 mm.

The 3D PET data were spatially coregistered and matched with the VINCI software onto the 3D CT data to obtain exact spatial co-registration of PET and CT data for subsequent accurate conversion of HU and LAC values. The high spatial resolution of the CT data serves as a positioning reference for the placement of the ROI to obtain the mean LAC values in the PET data. Figure 3 depicts the coregistration and positioning of ROIs in CT and PET data along two imaging planes to obtain volumes of interest (VOI) in the material samples (Figure 3). Thus, LAC values were measured over a volume of interest to average spatial inhomogeneities in the heterogeneous samples.

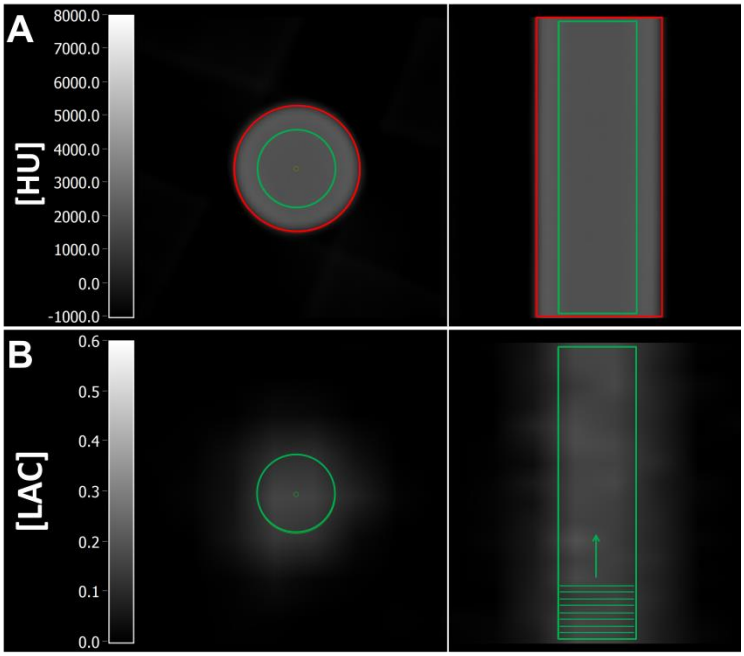

Figure 3: Definition of volumes-of-interest (VOI) to derive Hounsfield units (HU) from CT data (A), and linear attenuation coefficients (LAC) from PET transmission data (B). The example shows CT and PET data from homogeneous glass fiber reinforced epoxy (probe #26). Although all cylindrical material samples have an external diameter of 16 mm (red boundaries in transversal and coronal view in A), a centered VOI with a diameter of only 10 mm was selected (green) to reduce partial volume effects. The resulting VOI to measure HU in CT had a diameter of 16 mm (red boundaries in A), the resulting VOI to measure LAC in PET had a diameter of 10 mm (green boundaries in B).

Bilinear conversion

Equation 1 provides the bilinear conversion of CT HU values acquired at 140 kVp to PET LAC values at 511 keV as suggested by Carney et al.[18]

Eq. 1 For HU < 30 $y = 9.6 * 10^{-5} \times (HU + 1000)$

For HU > 30 $y = 5.64 * 10^{-5} \times (HU + 1000) + 4.08 * 10^{-2}$

Equation 2 provides the bilinear conversion of CT HU values acquired at 140 kVp to PET LAC values at 511 keV as suggested by Paulus et al.[19]

Eq. 2 $\text{For HU} < 30 \quad y = 9.6 * 10^{-5} \times (HU + 1000)$

$\text{For HU} > 30 \quad y = 5.75 * 10^{-6} \times (HU + 1000) + 9.2 * 10^{-2}$

The conversion, from the measured HU to LAC using the two bilinear conversions (Equation 1 and 2) and further post-processing steps, were all performed with MATLAB (MathWorks, Natick, US). The following post-processing steps were performed as described in more detail in Paulus et al. work.[19] To reduce the potential quantitative impact of minor streaking artifacts between neighboring samples on CT measurements (HU), for each sample the average HU value of surrounding artifacts was determined and subtracted from the measured HU for each sample. The masking of each circular sample was performed by thresholding with -600 HU and placing a circular mask on each sample. All residual background voxels exceeding the actual geometry of each sample were set to zero. Finally, a 4 mm Gauss filter was applied to all CT data for smoothing and matching the high spatial resolution of the CT data to the lower spatial resolution PET data.[19]

The two conversion methods according to Equations (1) and (2) are applied to the CT HU values as measured for each of the 38 material samples. Applying EQ (1) and (2) to the measured HU values leads to the corresponding LAC values for each material sample according to the two conversions suggested by Carney et al. and by Paulus et al. These two conversions serve as a reference in this study.

Additionally, the measured HU values and measured corresponding LAC for each of the 38 samples are plotted in an HU to LAC-conversion graph to result in a curve reflecting the CT and PET measurements of this study. By connecting the measured values with lines of best fit, an adapted equation for the HU to LAC conversion can be derived for the results. This can then be compared to the reference curves suggested by Carney et al. and by Paulus et al. To finally validate the measured HU to LAC conversion and to compare it to the two reference conversion methods, all three conversions are used to generate μmaps from CT data for both the heterogeneous and homogeneous material samples. To match the high spatial resolution of the CT data with the lower

spatial resolution of the PET detector (4.0 - 6.0 mm), a 4.0 mm Gaussian filter was applied during μmap generation. The three μmaps are then applied for attenuation correction of the material samples in PET/MR difference measurements.

PET/MR difference measurements

To evaluate and validate the effectiveness of the three different HU to LAC conversion methods, PET difference measurements were performed on an integrated 3-Tesla PET/MR whole-body hybrid imaging system (Biograph mMR, Siemens Healthcare GmbH, Erlangen, Germany). For this purpose, the cylindrical water phantom was filled with 18-F isotope to serve as a PET emission source. The phantom was positioned in the isocenter of the PET detector without any attenuation interference from the PET/MR patient table by mounting it free-floating at the head-end of the PET/MR patient table (Figure 4A).

The phantom activity (230 MBq in total, concentration 24 kBq/ml) and the extended acquisition time of 35 minutes in the phantom experiments were chosen to provide sufficient PET signal statistics. The setup without material samples served as the reference scan without any attenuation. The two sample holders were then consecutively placed onto the emission phantom (Figure 4B). Two PET emission measurements were carried out, one for each sample holder, to determine the 511 keV attenuation properties of each material sample. Both measurements were then time- and decay-corrected, to equalize the impact of tracer decay over time.

Thus, in the PET difference measurements, a PET emission measurement without attenuating samples served as a reference; two further PET emission measurements with attenuating samples surrounding the water emission phantom provide data to determine the attenuation at 511 keV of each sample. For subsequent evaluation of the three different HU to LAC conversion curves, the CT-based 3D attenuation maps of the heterogeneous and homogeneous phantom samples are applied for attenuation correction of the PET emission data of both phantoms. In the ideal situation, an

optimal conversion would provide absolute correction for the attenuation from all materials and would result in a homogeneous PET signal across the entire large volume water PET emission phantom. PET difference measurements between perfect attenuation corrected PET data with samples and the PET reference scan acquired without attenuating samples would, thus, result in zero difference across the water phantom.

The PET data were acquired in list mode. The reconstructed imaging matrix size was 344 x 344 x 127 with a voxel size of 2.09 x 2.09 x 2.03 mm^3. The reconstruction parameters of 3 subsets and 21 iterations correspond to the 3-dimensional ordinary Poisson ordered-subsets expectation maximization (3D OP-OSEM) reconstruction parameters.

For attenuation correction of the PET data for both material sample groups, three different hardware μmaps were used (1. Carney μmap, 2. Paulus μmap, 3. Oehmigen μmap).

Furthermore, the CT-based 3D template model of the cylindrical water phantom was used for attenuation correction of the phantom. The six AC PET data sets ($PET_{material}$) (two material groups, three μmaps for each material group) were then compared to the reference PET scan ($PET_{reference}$), where only the cylindrical water phantom was attenuation corrected, by calculating difference maps (Equation 3).

Eq. 3 $$relative\ difference\ maps = \frac{PET_{material} - PET_{reference}}{PET_{reference}} * 100\%$$

All post-processing steps and data reconstructions of the PET data were performed offline using the e7 tools software provided by the manufacturer of the PET/MR hybrid system.

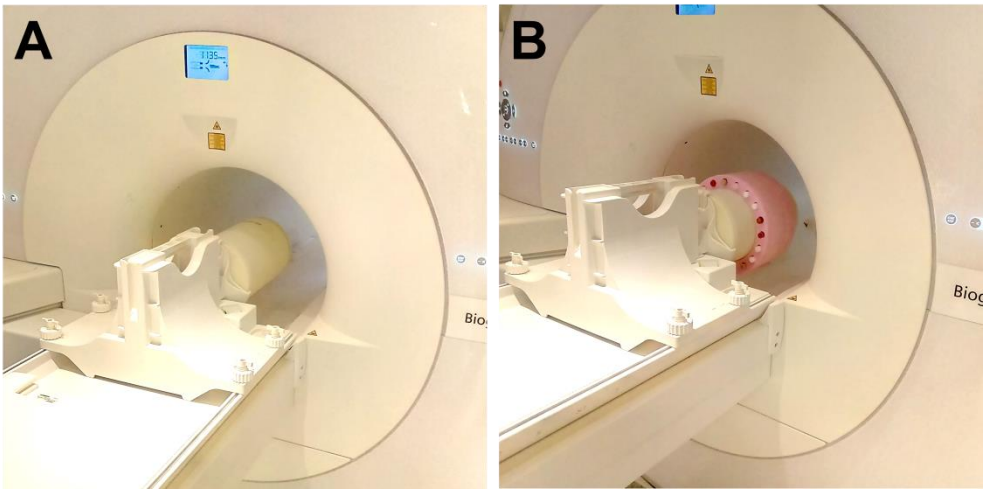

Figure 4: Setup for PET difference measurements in the PET/MR system. The large-volume water phantom injected with an 18-F isotope, which served as an emission source. Phantom holder (A) allows a free-floating positioning of the phantom in the isocenter of the PET/MR system. For the ensuing measurements the sample holders are positioned around the water phantom (B) and a second PET measurement is acquired.

Results

CT scans

Figure 5 shows the CT data of the two sample holders and the 38 different materials and corresponding µmaps. The 19 heterogeneous materials (upper row) can be depicted well due to the high spatial resolution of the CT scan. The homogeneous materials (lower row) can be depicted as regular shaped cylindrical structures with a smooth surface and homogeneous cross-sections (Figure 5).

PET transmission scans

The two consecutive 511 keV PET transmission scans of the 2x 19 material samples provide linear attenuation coefficients of all material samples. In Figure 5 all heterogeneous materials (upper row)

can be seen in the axial view of PET transmission images (right). The lowest measured LAC is PUR SG95 (polyurethane plates for RF coil housing manufacturing, sample #19) with 0.082 cm^{-1} ± 0.005 cm^{-1} LAC, whereas the highest attenuating heterogeneous material is soldering tin with 0.296 cm^{-1} ± 0.006 cm^{-1} LAC (sample #4).

Figure 5 depicts the axial view from PET transmission scans of the 19 homogenous material samples (lower row), where the high attenuating rods can be identified as copper and brass (samples #22 and #31). The measured LAC range from polyamide with a LAC of 0.0724 cm^{-1} ± 0.0034 cm^{-1} LAC (sample #33) to copper with 0.56 cm^{-1} ± 0.015 cm^{-1} LAC (sample #22).

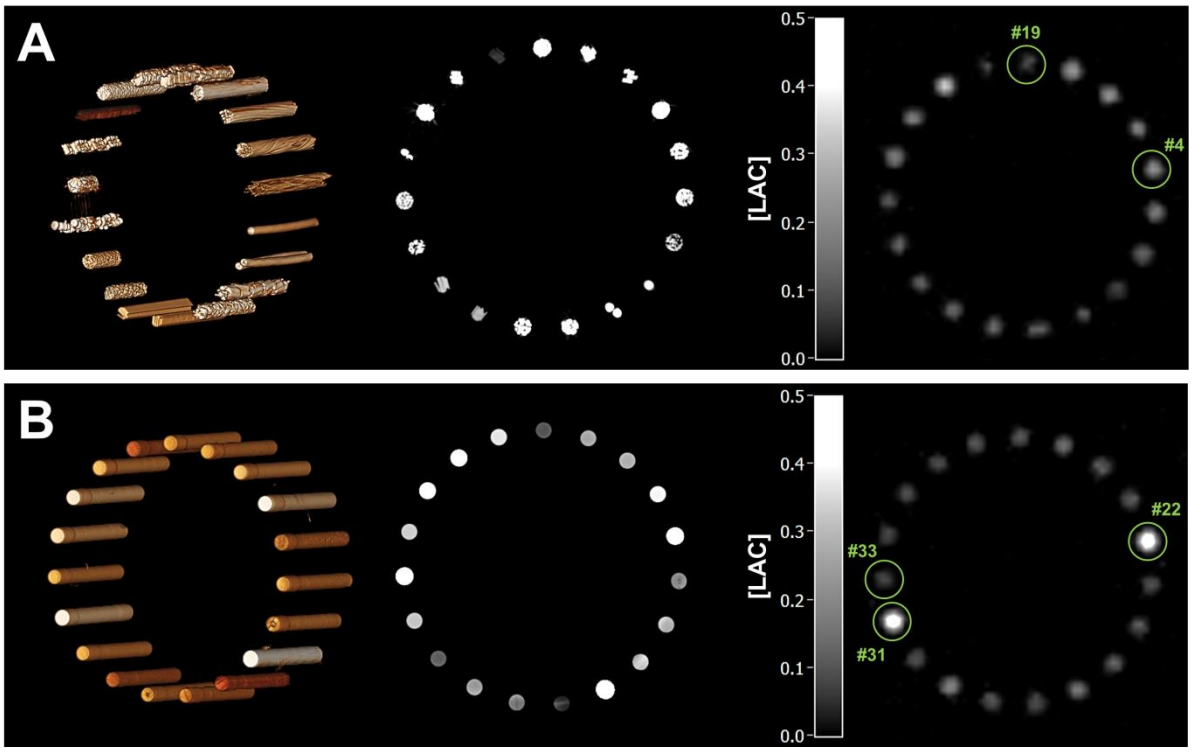

Figure 5: Upper row (A) provides CT data (left and middle) and PET transmission data (right) of the heterogeneous material samples #1-19. 3D renderings (left) and axial views (middle) depict the irregular shapes of the heterogeneous samples. Lower row (B) shows corresponding data of homogeneous samples #20-38.

The HU values for the different materials, given in Table 2, are measured mean values with their respective standard deviation.

Table 2 CT values and corresponding PET LAC

		CT data	Bilinear converted		PET data			CT data	Bilinear converted		PET data
no.	**Heterogeneous materials**	**[**HU**]** ± SD	**LAC [**cm^{-1}**]** Carney	**LAC [**cm^{-1}**]** Paulus	**LAC [**cm^{-1}**]** Oehmigen	**no.**	**Homogenous materials**	**[**HU**]** ± SD	**LAC [**cm^{-1}**]** Carney	**LAC [**cm^{-1}**]** Paulus	**LAC [**cm^{-1}**]** Oehmigen
#1	Capacitor, small dim.	7244 ± 383	0.506	0.139	0.185	**#20**	PVC	984 ± 3	0.153	0.103	0.101
#2	Capacitor, medium dim.	5200 ± 539	0.390	0.128	0.169	**#21**	TECAPET	270 ± 3	0.112	0.099	0.097
#3	Capacitor, large dim.	4805 ± 906	0.368	0.125	0.159	**#22**	Copper	24135 ± 3	1.458	0.237	0.561
#4	Soldering tin	12007 ± 138	0.774	0.167	0.297	**#23**	PC	108 ± 2	0.103	0.098	0.081
#5	Cable, K02252	4402 ± 39	0.345	0.123	0.151	**#24**	PMMA	127 ± 3	0.104	0.098	0.091
#6	Cable, 6Y-C6Y	3059 ± 84	0.270	0.115	0.131	**#25**	POM	339 ± 2	0.116	0.100	0.100
#7	Cable, DC wire	1563 ± 24	0.185	0.107	0.099	**#26**	GFK	1992 ± 11	0.210	0.109	0.116
#8	Cable 1TX / 8RX	3725 ± 12	0.307	0.119	0.127	**#27**	2-K Epoxid	45 ± 8	0.100	0.098	0.085
#9	Cable 2TX/2RX/6DC	4048 ± 25	0.326	0.121	0.135	**#28**	PEI	173 ± 5	0.107	0.099	0.091
#10	Inductor, large dim.	7730 ±1365	0.533	0.142	0.189	**#29**	Aluminium	2095 ± 7	0.215	0.110	0.146
#11	Inductor, small dim.	5803 ± 830	0.424	0.131	0.182	**#30**	PPSU	276 ± 2	0.113	0.099	0.092
#12	glass reinforced printed circuit board	1430 ± 18	0.178	0.106	0.103	**#31**	Brass	27464 ± 144	1.646	0.256	0.550
#13	Printed circuit boards FR4	1650 ± 25	0.190	0.107	0.115	**#32**	PEEK	194 ± 4	0.108	0.099	0.090
#14	Midi Spring Inductor	2772 ± 183	0.254	0.114	0.138	**#33**	PA	-57 ± 1	0.091	0.091	0.072
#15	Inductor 4700 nH	2444 ± 75	0.235	0,112	0.149	**#34**	PS	43 ± 2	0.100	0.098	0.078
#16	TX Trimmer	6807 ± 2203	0.481	0.137	0.168	**#35**	PE	97 ± 3	0.103	0.098	0.086
#17	PIN diode	12064 ± 615	0.778	0.167	0.268	**#36**	PVDF	632 ± 5	0.133	0.101	0.108
#18	Preamplifier	3703 ± 930	0.306	0.119	0.128	**#37**	ABS	-23 ± 5	0.094	0.094	0.077
#19	PUR SG95 SLM	144 ± 2	0.105	0.099	0.083	**#38**	PUR	182 ± 6	0.153	0.103	0.092

Table 2: All 38 materials with measured CT-based HU values and derived LAC values, by using two different bilinear conversion methods from Carney and Paulus. LAC values in the third column (Oehmigen) are measured values from this study.

365

Bilinear conversion

The measured LAC values of the material samples were matched to the corresponding HU values. Figure 6 shows an HU to LAC-conversion graph with three data sets, which are all based on the measured HU values of all 38 material samples. The use of the Carney conversion method provides
370 the highest slope in the HU to LAC conversion graph (blue crosses). The data points with the lowest slope (red circles) are Paulus converted LAC from measured CT-data HU. The third set of data points (green triangles) illustrates the acquired CT HU and the LAC from the PET transmission scans as obtained. The HU and LAC values were connected by a line of best fit to derive a corresponding conversion curve from the measured data points.

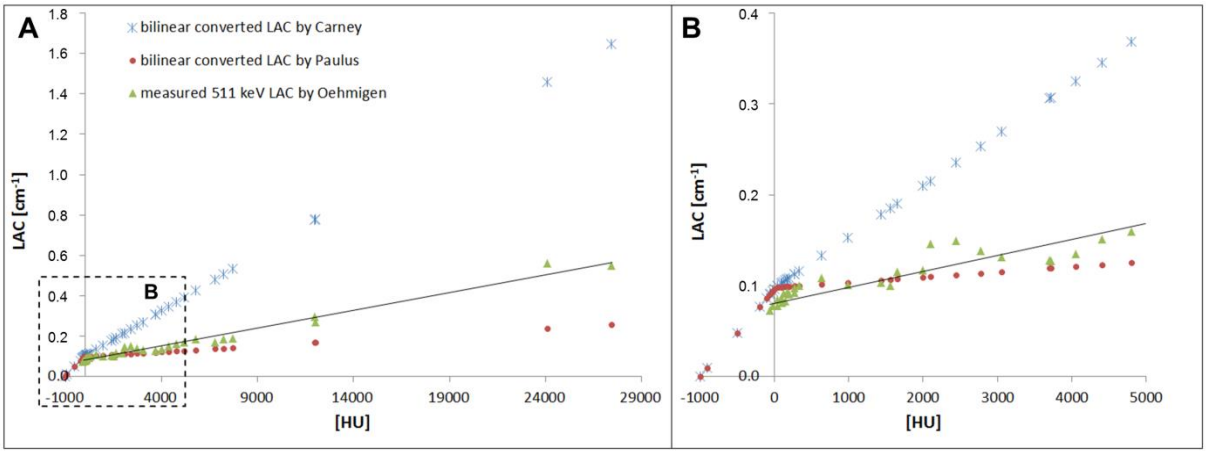

375

Figure 6: The line of best fit for the measured HU and LAC values (Oehmigen et al.) of the materials (green triangles) is located between the two calculated LAC values of Carney et al. (blue x's) and Paulus et al. (red circles). Note that the blue and red data points were not measured by Carney, nor by Paulus and colleagues .Instead, all data points were derived from the CT HU values of all material samples evaluated in this study by

applying the respective conversion curve by Carney et al. and by Paulus et al. Panel (B) shows a zoomed section for the lower HU and lower LAC values.

For the line of best fit of measured HU and LAC values, the slope and y-intercept are calculated and shown in Equation 4. According to the conversion curves by Carney et al. and Paulus et al., only HU values above HU +30 are considered. Consequently, ABS (material #37) with -23 HU and 0.077 cm^{-1} LAC together with PA (material #33) -57 HU and 0.072 cm^{-1} LAC were excluded from the graph. Only the remaining higher attenuating materials (> +30 HU) were included to derive the following equation. The left slope of the bi-linear curve was established by Carney et al., and was also used in the work by Paulus et al. Also in the present work, the left slope of the bi-linear curve was adopted from Carney et al.

Only the right slope of the bi-linear curve was derived and adapted from the results of the present study. Equation 4 provides the line of best fit for the measured LAC values depicted in Figure 6.

Eq. 4 For HU > 30 $y = 1.64 * 10^{-5} \times (HU + 1000) + 8.3 * 10^{-2}$

PET/MR difference measurements

The results of PET/MR phantom difference measurements are represented in Figure 7. The relative difference maps show the calculated difference (Equation 3) between the following two measurements: first, a measurement of the emission phantom, without any material samples (reference scan); and, second, a measurement with PET signal attenuating material samples placed around the emission phantom and with applied attenuation correction using the three different µmaps. The PET difference measurements with AC according to Carney et al. comes to a mean overall difference of 4.69 % ± 0.27 % as measured in a large circular ROI across the entire cross-section of the water phantom and measured in 60 slices along the z-axis of the phantom. Positive difference values and the associated red color in the phantom here indicate a resulting

overcorrection when applying Carney AC. Applying Paulus AC results in a mean difference of 2.84 % ± 0.72 % as measured within the water emission phantom volume. This indicates an undercorrection for Paulus AC.

Finally, applying the attenuation correction µmap as derived from HU and LAC measurements in this work leads to a low mean difference of 0.45 % ± 0.21 %, reflecting lower deviations between measured and true LAC values than for the Carney and Paulus conversions.

The line graphs in Figure 7 depict the variation of the mean difference measured in the circular ROI of each cross-sectional slice of the PET difference data sets along multiple slices over a distance of 120 mm along the z-axis of the phantom. These graphs show that the measured mean difference for the three conversions is relatively stable along the z-axis of the phantom.

The second row of Figure 7 represents the respective mean difference values for the homogeneous material samples. Carney AC shows a mean difference of 1.15 % ± 0.18 %. Paulus AC gives a mean difference of -2.67 % ± 0.25 %. Finally, applying the Oehmigen AC µmap as derived from HU and LAC measurements resulted in a low mean difference of 0.36 % ± 0.12 %.

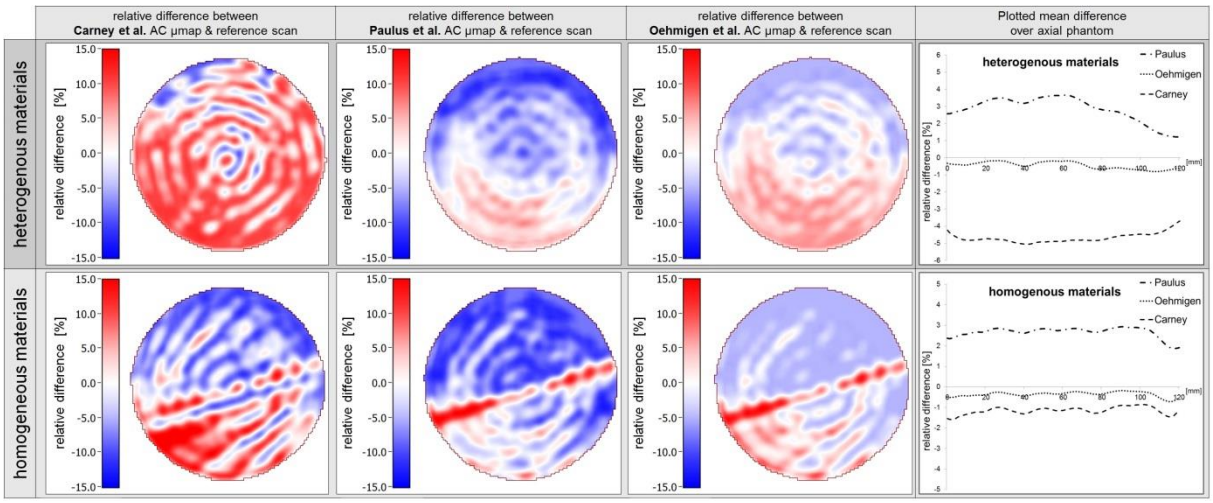

Figure 7: Calculated difference maps of PET scans are depicted. The first row shows the heterogeneous material sample results; the second row shows the homogeneous material sample results. Each difference map shows the relative difference of two PET scans, one with the phantom and material probes in comparison to a PET scan

without any material probes surrounding the phantom. The left column represents PET difference maps reconstructed with Carney AC; the second column represents difference maps reconstructed with Paulus AC, and the third column shows the reconstruction with the Oehmigen AC. Blue color indicates an undercorrection, whereas red color indicates overcorrection of the true attenuation values. Note that the red diagonal lines (strong overcorrection) across the phantom formed between the two metal samples in the lower row indicate methodological limits for attenuation correction of larger-size highly attenuating material (metal) samples.

Discussion

The current study systematically investigated both the CT and PET attenuation coefficients of a broad spectrum of materials covering a large range from low to highly attenuating materials. CT attenuation coefficients of highly attenuating materials were captured by using the extended HU-scale covering high values up to +30000 HU. The overlay of HU and LAC attenuation coefficients derived from the conversions by Carney et al., by Paulus et al. together with the measured attenuation coefficients derived from this research work reveals that the slope of the conversion curve derived from this study is in between the two previously published methods.[18,19] At the same time, the new conversion derived from this study is closer to the conversion suggested by Paulus et al. than it is to the PET/CT conversion proposed earlier by Carney et al..

CT

As expected, the standard deviations (SD) of measured HU in the homogeneous samples were low, whereas the measured HU in the heterogeneous samples shows a remarkably higher SD. The small dimensions of the collection of multiple electronic components in the test tubes leads to local HU maxima and HU minima, which result in higher SD when compared to the homogenous material samples (Table 2). As a limitation of the CT measurements, it has to be noted that the homogeneous metal samples with a diameter of 16 mm strongly attenuate the CT photons (copper with +24000 HU and brass with +27000 HU). In these situations, such high attenuation coefficients paired with a

rather large sample diameter may hamper accurate CT value reconstruction and can introduce artifacts. Thus, deviations between measured and real attenuation coefficients of the highly attenuating metal samples cannot be excluded.

PET

PET difference measurements serve as a highly sensitive validation experiment for the measured HU, measured LAC, and derived conversion curve. A large-volume (9.5 Liters) active emission phantom serves as reference for the PET measurement. Using the same phantom and identical position, a second PET measurement was taken with the modular phantom ring which included 19 heterogeneous or 19 homogeneous material samples. This however, will show lower activity values in the PET emission phantom due to the photon attenuation by various material samples surrounding the phantom. Under ideal conditions, reconstruction of the second PET scan with an appropriate attenuation correction will show a 0 % difference across the whole volume of the phantom between the two PET measurements. Creating µmaps according to the methods by Carney et al. and by Paulus et al., and subsequent use of the µmaps derived in this research lead to a visible and measurable PET quantification bias in the volume of the PET emission phantom (Figure 7). The blue color in the PET difference maps indicates a general undercorrection, whereas the red color indicates the overcorrection of the true attenuation coefficients of the various material samples. The red and blue color is not evenly distributed across the phantom volume (Figure 7). In general, the upper parts of the phantom show more blue color, while the lower parts of the phantom show more red color. This indicates that not all material samples are corrected according to their true attenuation coefficients when using the conversions by Carney et al. and by Paulus et al. (Figure 7, first and second column). When applying the conversion curve derived in this study to attenuation correction of heterogeneous and homogeneous materials, the overall PET difference bias across the phantom is much lower, as indicated by less red and blue color and by increased homogeneity across the phantom volume (Figure 7, third column). The last column represents the measured PET quantification bias across the phantom. As a result a large circular ROI was placed on the cross-

sectional view of the emission phantom and the overall bias within the ROI was determined. This was repeated for multiple transaxial slices along the z-axis of the phantom. The ROI measurements revealed a mean difference of 4.69 % ± 0.27 % (overcorrection) for the conversion of Carney et al. Applying the attenuation correction µmap according to Paulus et al. results in a mean difference -2.84 % ± 0.72 % (undercorrection). Finally, applying the attenuation correction µmap as derived from the HU and LAC measurements resulted in a reduced mean difference of 0.45 % ± 0.21 %, reflecting only low deviations. Due to these results, it should be emphasized that the large ROIs placed in the cross-sectional difference images of the emission phantom averages positive and negative bias. Local deviations close to a single material sample can be much higher (undercorrection or overcorrection). In clinical PET/MR applications, the resulting local bias in PET quantification can be much higher when, for example, SUV measurements are performed close to the attenuating structures of an RF coil that has not been corrected according to its "real" attenuation values. In this context, the faint red and blue color in the difference maps for the conversion derived indicates that each material sample (heterogeneous or homogeneous) was corrected with a derived attenuation value that is close to the true physical attenuation value.

Although the described AC methods provide correction factors for different materials and hardware components located within the FOV of the PET detector, the method of AC has general limitations when larger amounts of highly attenuating materials are to be corrected. Such samples irreversibly reduce the PET signal. Consequently, applying significant AC factors will amplify noise and introduce artifacts, which may hamper PET quantification in the resulting corrected images as when using the metal samples in Figure 7. Thus, the primary aim of designing RF coils and other hardware components for PET/MR hybrid imaging is to avoid excessive photon in advance. [24,25] This is achieved by using appropriate hardware design which avoids the placement of larger amounts of highly attenuating materials (e.g. metals) within the PET field-of-view. Only once an optimized and PET-transparent RF coil design has been constructed, can the remaining attenuation be corrected according to the method and conversion curve suggested in this study.

Such an elaborate experimental study involving numerous steps does come with potential limitations in each of the experimental steps. The development and realization of an experiment for conversion curve adaption involved several steps like the selection of appropriate material samples, phantom design and the execution of all measurements. The involved imaging modalities CT, PET, and PET/MR all come with inherent physical characteristics that need to be considered during planning and execution of an experiment. CT and PET data post-processing includes mathematical conversions, image co-registration, artifact removal, thresholding, and filtering. Furthermore, evaluation of the resulting CT and PET image data included ROI and VOI definition, averaging of attenuation coefficients, and HU to LAC conversion. Finally, the formation of μmaps and PET difference measurements require accurate spatial co-registration of all data. All of these listed factors and experimental steps may lead to systematic errors in the obtained results, despite thorough planning and execution of the experimental study.

Conclusion

An optimized method for the conversion of CT to PET attenuation coefficients has been derived by systematic measurement of 38 different materials frequently used in PET/MR hybrid imaging. In contrast to established methods, the new conversion also considers highly attenuating materials such as electronic components and metals, thus improving attenuation correction of hardware components in PET/MR hybrid imaging.

Compliance with Ethical Standards

Conflict of interest

The author Titus Lanz is an employee of Rapid Biomedical GmbH, Rimpar, Germany.

All other authors declare that there are no conflicts of interest.

Ethical approval

This article does not contain any studies with human participants performed by any of the authors.

References

1. Schütz L, Lobsien D, Fritzsch D, et al. Feasibility and acceptance of simultaneous amyloid PET/MRI. Eur J Nucl Med Mol Imaging. 2016 Nov;43(12):2236-2243.

2. Gatidis S, Bender B, Reimold M, Schäfer JF. PET/MRI in children. Eur J Radiol. 2017 Sep;94:A64-A70.

3. Nensa F, Bamberg F, Rischpler C, et al. Hybrid cardiac imaging using PET/MRI: a joint position statement by the European Society of Cardiovascular Radiology (ESCR) and the European Association of Nuclear Medicine. Eur Radiol. 2018 Oct;28(10):4086-4101.

4. Quick HH, von Gall C, Zeilinger M, Wiesmüller M, et al. Integrated whole-body PET/MR hybrid imaging: clinical experience. Invest Radiol. 2013;48:280-289.

5. Paulus DH, Thorwarth D, Schmidt H, Quick HH. Towards integration of PET/MR hybrid imaging into radiation therapy treatment planning. Med Phys. 2014 Jul;41(7):072505.

6. Paulus DH, Oehmigen M, Grüneisen J, Umutlu L, Quick HH. Whole-body hybrid imaging concept for the integration of PET/MR into radiation therapy treatment planning. Phys Med Biol. 2016 May 7;61(9):3504-3520.

7. Paulus DH, Braun H, Aklan B, Quick HH. Simultaneous PET/MR imaging: MR-based attenuation correction of local radiofrequency surface coils. Med Phys. 2012; 39:4306-4315.

8. MacDonald LR, Kohlmyer S, Liu C, Lewellen TK, Kinahan PE. Effects of MR surface coils on PET quantification. Med Phys. 2011;38:2948-2956.

9. Tellmann L, Quick HH, Bockisch A, Herzog H, Beyer T. The effect of MR surface coils on PET quantification in whole-body PET/MR: Results from a pseudo-PET/MR phantom study. Med Phys. 2011;38:2795-2805.

10. Delso G, Martinez-Möller A, Bundschuh RA et al. Evaluation of the attenuation properties of MR equipment for its use in a whole-body PET/MR scanner. Phys Med Biol. 2010 Aug 7;55(15):4361-4374.

11. Boellaard R, Rausch I, Beyer T, Delso G, Yaqub M, Quick HH, Sattler B. Quality control for quantitative multicenter whole-body PET/MR studies: A NEMA image quality phantom study with three current PET/MR systems. Med Phys. 2015 Oct;42(10):5961-5969.

12. Ziegler S, Jakoby BW, Braun H, Paulus DH, Quick HH. NEMA image quality phantom measurements and attenuation correction in integrated PET/MR hybrid imaging. EJNMMI Phys. 2015 Dec;2(1):18.

13. Martinez-Möller A, Souvatzoglou M, Delso G, et al. Tissue classification as a potential approach for attenuation correction in whole-body PET/MRI: evaluation with PET/CT data. J Nucl Med. 2009;50:520–526.

14. Schulz V, Torres-Espallardo I, Renisch S, et al. Automatic, three-segment, MR-based attenuation correction for whole-body PET/MR data. Eur J Nucl Med Mol Imaging. 2011 Jan;38(1):138-152.

15. Paulus DH, Quick HH, Geppert C, et al. Whole-Body PET/MR Imaging: Quantitative Evaluation of a Novel Model-Based MR Attenuation Correction Method Including Bone. J Nucl Med. 2015;56:1061-1066.

16. Oehmigen M, Lindemann ME, Gratz M, et al. Impact of improved attenuation correction featuring a bone atlas and truncation correction on PET quantification in whole-body PET/MR. Eur J Nucl Med Mol Imaging. 2018 Apr;45(4):642-653.

17. Kinahan PE, Townsend DW, Beyer T, Sashin D. Attenuation correction for a combined 3D PET/CT scanner. Med Phys. 1998 Oct;25(10):2046-2053.

18. Carney et al. Method for transforming CT images for attenuation correction in PET/CT imaging. Med Phys. 2006;33:976-983.

19. Paulus DH, Tellmann L, Quick HH. Towards improved hardware component attenuation correction in PET/MR hybrid imaging. Phys Med Biol. 2013;58:8021-8040.

20. Hofmann M, Bezrukov I, Mantlik F, et al. MRI-based attenuation correction for whole-body PET/MRI: quantitative evaluation of segmentation- and atlas-based methods. J Nucl Med. 2011 Sep;52(9):1392-1399.

21. Mehranian A, Zaidi H. Emission-based estimation of lung attenuation coefficients for attenuation correction in time-of-flight PET/MR. Phys Med Biol. 2015 Jun 21;60(12):4813-4833.

22. Rezaei A, Deroose CM, Vahle T, Boada F, Nuyts J. Joint Reconstruction of Activity and Attenuation in Time-of-Flight PET: A Quantitative Analysis. J Nucl Med. 2018 Oct;59(10):1630-1635.

23. Torrado-Carvajal A, Vera-Olmos J, Izquierdo-Garcia D et al. Dixon-VIBE Deep Learning (DIVIDE) Pseudo-CT Synthesis for Pelvis PET/MR Attenuation Correction. J Nucl Med. 2019 Mar;60(3):429-435.

24. Quick HH. Integrated PET/MR. J Magn Reson Imaging. 2014;39:243-258.

25. Paulus DH, Quick HH. Hybrid Positron Emission Tomography/Magnetic Resonance Imaging: Challenges, Methods, and State of the Art of Hardware Component Attenuation Correction. Invest Radiol. 2016 Oct;51(10):624-634.

26. Burger, C., Goerres, G., Schoenes., et al. PET attenuation coefficients from CT images: experimental evaluation of the transformation of CT into PET 511-keV attenuation coefficients. Eur J Nucl Med Mol Imaging 2002 29: 922-927.

27. Ay, M. R., Shirmohammad, M., Sarkar, S., Rahmim, A., Zaidi, H.. Comparative assessment of energy-mapping approaches in CT-based attenuation correction for PET. Mol Imaging Biol 2011 13:187-198.

28. Xia, T., Alessio, A. M. and Kinahan, P. E.. Dual energy CT for attenuation correction with PET/CT. Med Phys 2014 41:012501.

29. Teimourian, B., Ay, M. R., Shamsaie Zafarghandi, M., et al. A novel energy mapping approach for CT-based attenuation correction in PET. Med Phys 2012 39:2078-2089.

30. Vollmar S, Cizek J, Sué M, et al. VINCI -Volume Imaging in Neurological Research, Co-Registration and ROIs included, Forschung und wissenschaftliches Rechnen 2003 (Kremer K, Macho V, eds), Göttingen: GWDG (2004) 115-131.

31. Wienhard K, Dahlbom M, Eriksson L, et al. The ECAT EXACT HR: performance of a new high resolution positron scanner. J Comput Assist Tomogr 1994 Jan-Feb;18(1):110-118.

32. Brix G, Zaers J, Adam LE, et al. Performance evaluation of a whole-body PET scanner using the NEMA protocol. National Electrical Manufacturers Association. J Nucl Med. 1997 Oct;38(10):1614-1623.